Aerodynamic and Structural Analysis of a Low-Speed Campus Delivery Robot

Erik Ardiansyah[1*], Anugerah Wibisana [1]

[1]Department of Electrical Engineering, Robotics Engineering Technology Study Program,
Politeknik Negeri Batam, Batam, Indonesia

[*]Email: erikardiansyah253@gmail.com

Received on dd-mm-yyyy | Revised on dd-mm-yyyy | Accepted on dd-mm-yyyy

***Abstract*— This study presents a numerical evaluation of the aerodynamic performance and structural integrity of a low-speed campus delivery robot design using Computational Fluid Dynamics (CFD) and Finite Element Analysis (EA) methods. CFD simulations were conducted at speeds ranging from 0.5 m/s to 10.0 m/s to analyze airflow characteristics and drag forces. The results show that drag force increases quadratically with speed, from 0.2091 N at 0.5 m/s to 12.9906 N at 10.0 m/s, but remains efficient within typical campus operating speeds. FEA analysis under vertical loads of 5–15 kg confirmed the structural strength of the 6061 aluminum frame: at the maximum 15 kg load, the peak stress was only 3.207 MPa, well below the material's yield strength, with a maximum deformation of 4.527×10^{-3} mm and a minimum Factor of Safety (FOS) of 85.7, indicating the design is overdesigned relative to its operational load. Future improvement is recommended through frontal-shape optimization and selective thickness reduction in low-stress regions to reduce overall weight without compromising stability.**

Keywords: Computational Fluid Dynamics (CFD), Drag Coefficient, Factor of Safety, Finite Element Analysis (FEA), Robot Delivery.

I. INTRODUCTION

The rapid development of autonomous technology has significantly changed last-mile delivery systems, especially in confined environments such as campuses. The use of autonomous delivery robots is an innovative solution to improve logistics efficiency while reducing dependence on human labor. Although these robots generally operate at low speeds, energy efficiency remains a major challenge due to the limited capacity of the batteries used to support the navigation, sensor, and drive systems. In this context, aerodynamic effects—especially air resistance—emerge as a crucial technical factor. Unoptimized air resistance can increase the motor's workload, which directly results in wasted battery energy consumption and shortens the robot's operational range. Therefore, aerodynamic testing from the design stage is essential to ensure that the robot has long operational endurance in a dynamic campus environment.

Previous studies have shown that vehicle body optimization effectively reduces the drag coefficient (CD) [1], and that additional components such as spoilers and diffusers can significantly alter airflow characteristics [2], [3]; more recent work on passive drag reduction for complex commercial vehicle geometries has further confirmed that shape optimization of the front and cab regions can substantially lower aerodynamic resistance even without active flow-control devices [4]. Beyond aerodynamics, the structural integrity of a robot frame under logistical loads is a critical safety concern, as structural failure due to overload may cause severe operational issues [5]. This concern is reinforced by recent finite element studies on vehicle and platform chassis, which show that stress distribution and factor-of-safety evaluation are essential for validating structural reliability under both static and dynamic loading conditions, and that material selection and lightweight optimization strongly influence the resulting safety margin [6], [7], [8]. Campus delivery robots also require a robust mechanical platform to support reliable perception systems; for example, Simanjuntak and Wibisana [9] developed a YOLOv5n-based depth camera system for safe human–robot interaction, which necessitates a structurally sound and aerodynamically efficient robot body.

Therefore, this study aims to conduct an in-depth numerical analysis of air resistance and stress distribution in the design of a campus delivery robot as part of an integrated robot development cycle. Using Computational Fluid Dynamics (CFD), air flow characteristics and drag forces are evaluated to determine the aerodynamic efficiency limits of the robot body at various speed ranges. Simultaneously, Finite Element Analysis (FEA) is applied to validate the strength of the frame in withstanding varying loads, in order to prevent the risk of permanent deformation. The main contribution of this study is to provide comprehensive technical data as a guide for design optimization prior to the manufacturing stage, resulting in a robot that is not only energy efficient through good aerodynamic performance, but also has reliable structural durability to support various smart sensor devices in the future.

II. METHOD

This study employs a numerical approach using two main methods: Computational Fluid Dynamics (CFD) and Finite Element Analysis (FEA). CFD was applied to analyze airflow behavior and drag characteristics of the robot body at speeds ranging from 0.5 m/s to 10 m/s, following a systematic validation framework to ensure accurate wall effect resolution [10], consistent with recent CFD-based approaches used to evaluate aerodynamic and hydrodynamic drag on robotic platforms using SolidWorks Flow Simulation [11], [12]. Meanwhile, FEA was used to predict the structural response of the robot frame under static loading conditions, as commonly applied in material behavior analysis [13], including recent extended finite element studies on stress intensity in aluminum components [15], frame structure optimization using FEA [15], and multiphysics optimization of load-bearing vehicle frames for weight reduction [16]. Simulations were conducted using SolidWorks to obtain von Mises stress, deformation, and Factor of Safety (FOS) values, adopting approaches similar to previous studies on wheeled robot frame strength and performance comparison [16], [17], as well as recent structural assessments of electric vehicle chassis using finite element analysis [18].

Robot geometry was initially developed in a three-dimensional CAD environment to represent actual dimensions and structural components with precision, ensuring that the model is ready for high-fidelity numerical discretization [19]. In CFD analysis, the appropriate boundary conditions are strictly defined, including varying inlet velocity, static pressure, and no-slip wall conditions on the entire surface of the robot to simulate realistic air interactions [20]. A thorough mesh independence study was conducted to ensure that the simulation results had reached convergence and were no longer affected by element size variations, thereby improving data validity as required in standard aerodynamic assessments [21].

Turbulence effects were considered using appropriate turbulence models, such as k-epsilon or k-omega SST, to capture the phenomena of flow separation and wake formation behind the robot body, which are often the main sources of drag [22]. This approach is crucial for understanding the impact of body geometry on energy consumption in autonomous platforms [23]. Crucial aerodynamic parameters, including surface pressure distribution, velocity contours, and total drag force, are systematically extracted to ensure that the robot meets both structural and efficiency standards for campus logistics applications [24]. The entire series of methodologies and research workflows, from modeling to data collection, are illustrated in detail in Figure 1.

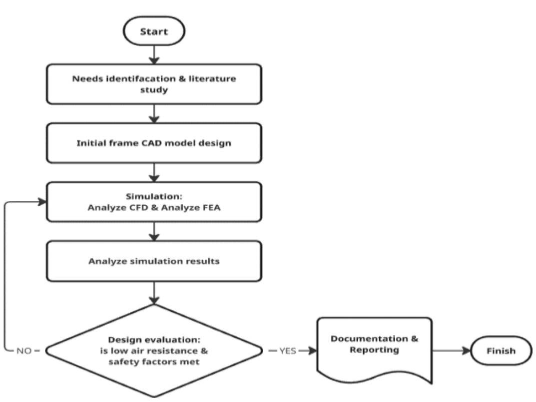

Figure 1 *Flow diagram*

A. Geometric Design of Delivery Robot

The 3D modeling of the delivery robot frame was developed based on operational requirements, with em-phasis on structural strength, durability, and load-bearing capability. The frame was designed to support all robot components, including the drive system, bat-teries, and cargo container, while ensuring proper load distribution to prevent excessive stress. Several de-sign alternatives were evaluated to identify the most ef-ficient and reliable configuration. The final 3D model was created using SolidWorks 2022 by defining the di-mensions, configuration, and joint placement of each frame element, resulting in an optimized structure suita-ble for campus delivery operations, as shown in Figure 2.

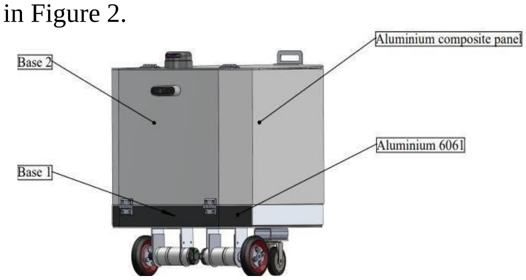

Figure 2 *Current view of the Standard frame*

The standard frame design shown in Figure 2 con-sists of two parts, namely the upper base where food is stored and the lower base where the entire electrical circuit is stored. The main material used is a combina-tion of aluminum composite panel and hollow alumi-num 6061.

B. Frame Material Selection

The selection of materials for the robot's main structure is based on a balance between weight and strength. Aluminum 6061 was chosen as the main frame because it has an excellent strength-to-weight ratio and high corrosion resistance, which is important for outdoor operations, including an elastic modulus of 69,000 N/mm², a yield strength of 276 N/mm², and a low thermal expansion coefficient of 2.4×10^{-5} /K. Aluminum 5052-H32 and aluminum 6063-T5 are used as supporting materials to provide additional structural stability, while Aluminum Composite Panel (ACP) is used as the body cover due to its lightweight and malleable properties, enabling it to protect internal electronic components without adding significant overall mass, as summarized in Table 1.

Table I
Material Properties

Properties (Units)	Aluminum Composite Panel (ACP)	Aluminum 6061	Aluminum 5052-H32	Aluminum 6063-T5
Elastic Modulus (N/mm^2)	5.5×10^4	6.9×10^4	7.0×10^4	6.9×10^4
Poisson's Ratio (N/A)	0.30	0.33	0.33	0.33
Shear Modulus (N/mm ^2)	3.19×10^4	2.60×10^4	2.61×10^4	2.59×10^4
Mass Density (Kg/m^3)	1450	2700	2680	2700
Tensile Strength (N/mm^2)	55	310	228	145
Yield Strength (N/mm^ 2)	40	276	193	110
Thermal Expansion Coefficient (/K)	2.30×10^{-5}	2.40×10^{-5}	2.38×10^{-5}	2.34×10^{-5}

Aerodynamic analysis was conducted using Computational Fluid Dynamics (CFD) in SolidWorks Flow Simulation to evaluate the air resistance characteristics of the delivery robot body, including drag force, pressure distribution, and drag coefficient. The fluid domain surrounding the robot was discretized into mesh elements to ensure accurate flow simulation. Simulations were performed at five airflow velocities—0.5 m/s, 1.5 m/s, 2.5 m/s, 5.0 m/s, and 10.0 m/s—to examine the effect of speed variation on the robot's aerodynamic behavior and stability.

C. Setting Parameters and Running CFD Simulation Analysis

Aerodynamic analysis was conducted using Computational Fluid Dynamics (CFD) in SolidWorks Flow Simulation to evaluate the air resistance characteristics of the delivery robot body, including drag force, pressure distribution, and drag coefficient. The fluid domain surrounding the robot was discretized into mesh elements to ensure accurate flow simulation. Simulations were performed at five airflow velocities—0.5 m/s, 1.5 m/s, 2.5 m/s, 5.0 m/s, and 10.0 m/s—to examine the effect of speed variation on the robot's aerodynamic behavior and stability.

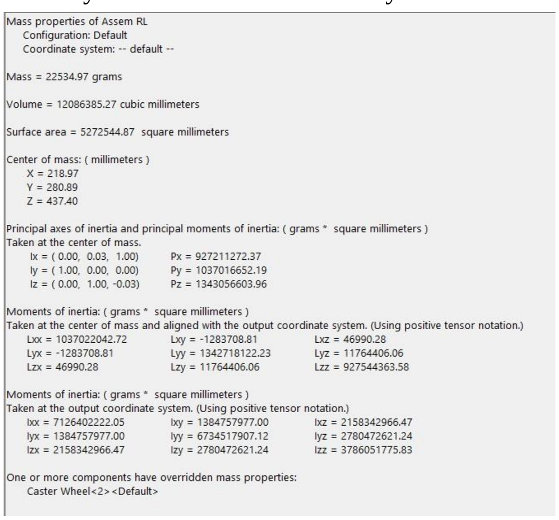

Figure 3 *Mass properties the robot*

Figure 3 shows the mass properties of the robot obtained through CAD software. The information displayed includes total mass, volume, surface area, and the position of the center of mass in a three-dimensional coordinate system. In addition, this figure also presents the principal axes of inertia along with the values of moment of inertia on each axis, both referenced to the center of mass and the global coordinate system. This data provides an overview of the robot's overall mass distribution, which is very important for analyzing stability, balance, and dynamic response during movement. By knowing the position of the center of mass and inertia characteristics, the robot design can be evaluated to ensure safe mechanical performance and support structural and aerodynamic simulation results in the next stage of analysis.

The calculation of the Drag Coefficient (C_D) is done automatically using the Equation Goal feature in SolidWorks Flow Simulation. The value () C_D is obtained by entering the parameter of the frontal projection area as measured by the dimensions of the robot into the following equation, where the frontal area A = 0.1894 m² (obtained from projected dimensions of 494.65 mm × 382.94 mm):

$$F_d = \frac{1}{2} \rho\, v^2\, C_d\, A \qquad (1)$$

According to formulated in Equation 1, drag force is directly proportional to the square of velocity (v^2). This explains why the jump in drag force at a velocity of 10.0 m/s is almost 60 times greater than at a velocity of 0.5 m/s. Where F_d is the drag force (N), ρ is the air density (kg/m^3), v is the air flow velocity (m/s), C_d is the drag coefficient, and A is the frontal area of the robot (m^2).

Table II
List of Speed Parameters and Air Resistance Cal-culation Formula in CFD Simulation

Speed (V)	**Speed Square (V2)**	**Denominator Constant (ρ·V2·A)**
0.5 m/s	0.25	0.0580
1.5 m/s	2.25	0.5221
2.5 m/s	6.25	1.4497
5.0 m/s	25.0	5.7988
10.0 m/s	100.0	23.1956

The table 2 illustrates the effect of increasing velocity on air resistance parameters calculated in SolidWorks. As the speed increases from 0.5 m/s to 10.0 m/s, both the squared velocity and the denominator constant rise significantly, forming the basis for automatic drag force calculations using SG Force to evaluate the aerodynamic efficiency of the design at different speeds.

D. Setting Parameters and Running FEA Simulation

Storage box durability was analyzed using Finite El-ement Analysis (FEA) in SolidWorks Simulation to evaluate stress, displacement, and factor of safety un-der vertical loading. ACP and aluminum materials were defined based on their mechanical properties, while the model's mass properties were obtained using the Mass Properties feature, as shown in Figure 4.

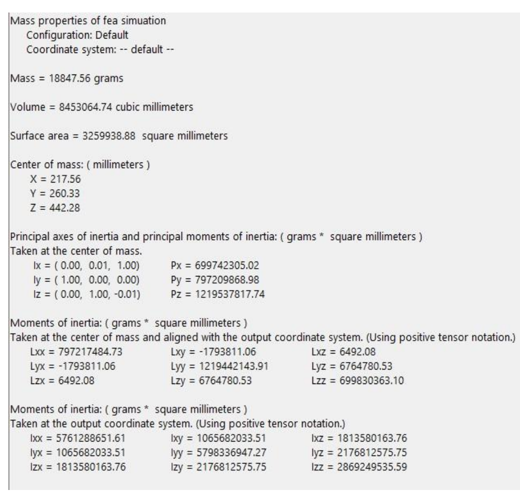

Figure 4 *Mass properties the robot*

Three vertical loading scenarios of 5 kg, 10 kg, and 15 kg were applied to the top surface of the storage box to represent the unloaded, partial-load, and maximum operational-load conditions, respectively, with the bottom surface defined as fixed geometry and panel connections modeled as bonded. The simulation results are presented as stress contours, displacement, and safety factor distributions to assess the structural integrity of the storage box.

The boundary conditions in the CFD simulation are set to represent the actual campus environment. Air is assumed to be an incompressible fluid under standard conditions ($25 \circ C$). For the FEA simulation, vertical loads (5 kg, 10 kg, and 15 kg) are applied evenly to the upper surface of the storage area, while the wheels or lower supports are set as fixed geometry to simulate static conditions when carrying loads. the implementation of this boundary condition is illustrated in the following figure 5.

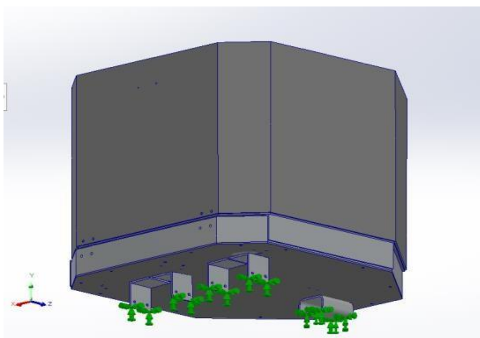

***Figure 5** Fixed Geometry for Boundary Condition*

E. Meshing Process and Quality Assessment

The meshing process discretizes the robot frame into small elements to enable numerical load distribution analysis. Tetrahedral solid elements were used to accurately represent complex 3D geometry, with global element sizes defined by the overall frame dimensions and local mesh refinement applied to critical regions such as joints, connecting plates, and mounting points to capture stress concentrations. The global mesh configuration is shown in the following figure 6.

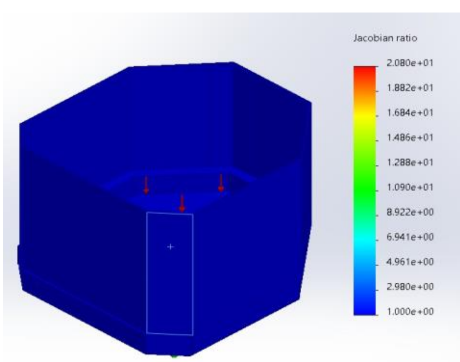

***Figure 6** Global Mesh Robot Frame*

Mesh quality was evaluated to ensure minimal element distortion and reliable simulation accuracy using a Jacobian ratio assessment with 16 sampling points per element. The Jacobian values ranged from 1.00 to 29.64, remaining below the SolidWorks recommended limit (≤40), indicating good numerical stability. Additionally, more than 85% of the elements exhibited an aspect ratio below 3 with no distorted elements detected, confirming the mesh as high quality and suitable for structural analysis. A summary of the mesh configuration, including element type, size, number of elements and nodes, and key quality indicators, is presented in the following figure 7.

Mesh Details:
Study name: beban 10kg* (-Default-)
Mesh type: Solid Mesh
Mesher Used: Blended curvature-based mesh
Jacobian points for High quality mesh: 16 points
Max Element Size: 50 mm
Min Element Size: 2.5 mm
Mesh quality: High
Total nodes: 103188
Total elements: 54420
Maximum Aspect Ratio : 53.872
Percentage of elements\with Aspect Ratio < 3 : 77.2
Percentage of elements\with Aspect Ratio > 10 : 4.8
Percentage of distorted elements : 0
Number of distorted elements:0
Remesh failed parts independently: Off
Time to complete mesh(hh;mm;ss): 00:00:21
Computer name:

***Figure 7** Mesh Summary*

The simulation employed a solid mesh with a blended curvature-based approach and Jacobian evaluation at 16 points per element. The maximum and minimum element sizes were set to 50 mm and 2.5 mm, respectively, resulting in a mesh of 54,420 elements and 103,188 nodes, which provides adequate discretization for structural analysis. Mesh quality assessment showed no distorted elements, with 77.2% of elements having an aspect ratio below 3 and 10.4% below 10; despite a maximum aspect ratio of 53.87, the overall mesh quality remains within acceptable limits for static analysis and is considered stable for finite element simulations.

The first simulation carried out was a stress analysis, which identified the stress distribution on the frame under operational load. This helps determine areas of high voltage that can cause material failure. The voltage that occurs on an object can be formulated as (2).

$$\sigma = \frac{F}{A} \quad (2)$$

Where σ represents stress or force per unit area (N/m²), F represents force (N), and A represents cross-sectional area (m²). The second simulation is displacement analysis, which evaluates how the frame deforms under load. Excessive displacement can disrupt the balance and stability of the robot during operation; therefore, this analysis ensures the frame maintains sufficient rigidity for stable operation. The displacement that occurs in an object can be formulated as (3).

$$E = \frac{\sigma}{\varepsilon} \quad (3)$$

Where E represents the Modulus of elasticity, σ represents Tension (N/m²), and ε represents Strain. The third simulation is safety factor analysis (FOS), which is used to assess the safety margin of the frame under load. FOS represents the ratio between the applied stress and the strength of the material before permanent deformation. This analysis highlights areas with low safety margins, guiding designers to modify or strengthen components to ensure reliability. The FOS that occurs on an object can be formulated as (4).

$$\eta = \frac{\Sigma y}{x} \quad (4)$$

Where Ƞ represents the Safety Factor, sy represents the Yield Strength of the material (N/m²), and σ represents the Maximum von Mises Voltage.

III. RESULT AND DISCUSSION

This section presents the results of the CFD and FEA simulations described in Section II, covering aerodynamic drag characteristics at varying airflow velocities and structural performance under three vertical loading scenarios.

A. *CFD Simulation Pressure Scenario*

The simulation was conducted using an external fluid flow approach, with the robot body fixed within the computational domain. Airflow velocities ranging from 0.5 m/s to 10 m/s along the Z-axis represent the robot's operating speed relative to ambient air, enabling analysis of airflow interaction with the robot surface under realistic operating conditions.

1) *Airflow Visualization and Pressure Distribution Analysis*

The initial analysis examined airflow interaction with the robot body surface, where pressure distribution was strongly influenced by the front geometry that is nearly perpendicular to the flow direction. Quantitative evaluation was performed by extracting drag force along the Z-axis and drag coefficient values from the Goal Plots, which are essential for assessing the energy efficiency of the robot body design at different operating speeds.

The aerodynamic results were subsequently evaluated across the tested velocity range to identify the relationship between operating speed and the resulting aerodynamic resistance. As the inlet velocity increased, changes in the flow field around the robot body affected the magnitude of the pressure and viscous forces acting on its surface. The comparison of drag force and drag coefficient at each operating condition provides a basis for determining the aerodynamic behavior of the robot and identifying the speed range in which the body design can maintain acceptable aerodynamic performance. These results were then used as a reference for evaluating the potential influence of aerodynamic resistance on the overall energy efficiency of the campus delivery robot.

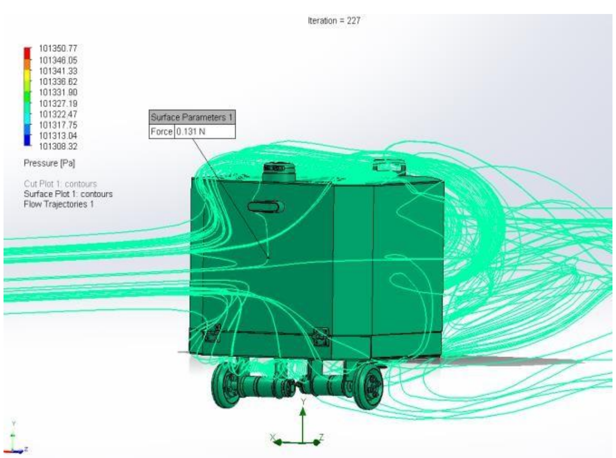

***Figure 8** Visualization Surface Plot and Flow Trajectories Speed 0.5 m/s*

The visualization in Figure 8 shows the surface pressure distribution (surface plot) and flow trajectories at a low operating speed of 0.5 m/s.

Table III
Results of Force Convergence in the 0.5 m/s Simulation

Parameters	Unit (N)	Averaged Value	Minimum Value	Maximum Value	Convergence
SG Force (Y)	N	0.0399	0.0380	0.0413	Yes
SG Force (Z)	N	0.2091	0.2085	0.2100	Yes
Total Force Equation	N	0.8013	0.7987	0.8044	Yes

Based on the data in Table 3, the average drag coefficient on the Z-axis (SG Force Z) was recorded at 0.2091 N. At this speed, the airflow appears to be very stable passing through the robot body with minimal pressure accumulation at the front, indicating high energy efficiency for initial movement.

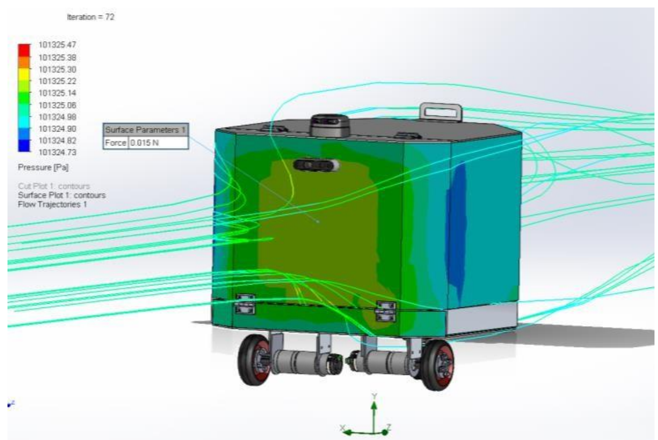

***Figure 9** Visualization Surface Plot and Flow Trajectories Speed 1.5 m/s*

The increase in speed to 1.5 m/s, as shown in Figure 7, did not show any drastic changes in the air flow pattern.

Table IV
Results of Force Convergence in the 1.5 m/s Simulation

Parameters	Unit (N)	Averaged Value	Minimum Value	Maximum Value	Convergence
SG Force (Y)	N	0.0399	0.0381	0.0414	Yes
SG Force (Z)	N	0.2092	0.2085	0.2100	Yes
Total Equation	N	0.8013	0.7987	0.8045	Yes

The data in Table 4 shows that the SG Force (Z) value is stable at 0.2092 N. This indicates that at low speeds, the robot design is able to maintain its aerodynamic characteristics without creating significant additional drag.

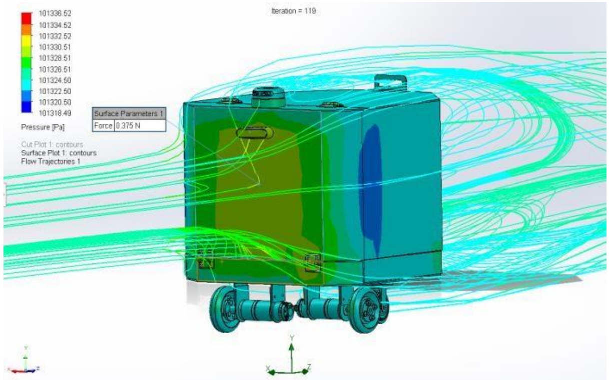

Figure 10 *Visualization Surface Plot and Flow Trajectories Speed 2.5 m/s*

At a speed of 2.5 m/s (Figure 10), a more measurable increase in drag force began to be observed.

Table V
Results of Force Convergence in the 2.5 m/s Simulation

Parameters	Unit (N)	Averaged Value	Minimum Value	Maximum Value	Convergence
SG Force (Y)	N	0.0395	0.0260	0.0528	Yes
SG Force (Z)	N	0.5943	0.5933	0.5965	Yes
Total Force Equation	N	0.8199	0.8185	0.8230	Yes

Table 5 shows that the average SG Force (Z) value increased to 0.5943 N. Although the wind load began to increase, the airflow pattern still followed the contours of the robot body well, and the maximum pressure remained concentrated on the flat surface of the front.

.

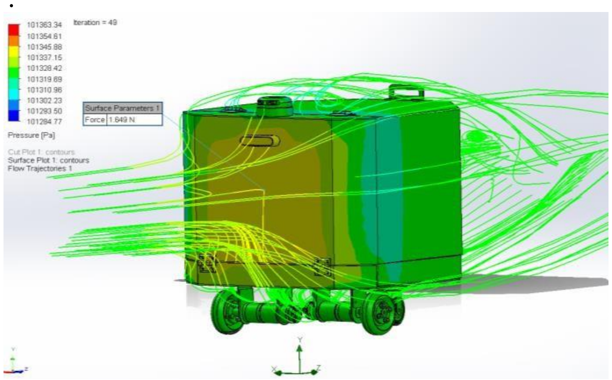

Figure 11 *Visualization Surface Plot and Flow Trajectories Speed 5.0 m/s*

Figure 11 shows a visualization at a moderate speed of 5.0 m/s, where airflow disturbances around the sharp edges of the robot begin to appear more clearly. At this speed, air resistance can no longer be ignored, as the pressure gradient between the front and rear areas begins to increase. This visualization captures the initial formation of small vortices at the corners of the upper box, indicating that the robot's non-aerodynamic shape is beginning to affect the overall stability of the airflow.

Table VI
Results of Force Convergence in the 5.0 m/s Simulation

Parameter	Unit (N)	Averaged Value	Minimum Value	Maximum Value	Convergence
SG Force (Y)	N	0.6440	0.6070	0.6677	Yes
SG Force (Z)	N	2.1590	2.1281	2.1976	Yes
Total Force Equation	N	0.7446	0.7340	0.7579	Yes

Based on the data presented in Table 6, there is a significant increase in drag force to 2.1590 N when the robot reaches a speed of 5.0 m/s. Physically, this phenomenon indicates that at medium speeds, the robot's geometric profile begins to experience more complex fluid resistance than at low speeds. Technically, this increase in drag force is directly proportional to the square of the speed, which means that air resistance becomes a critical variable that affects battery energy consumption. This shows that as the operational speed increases, the workload on the actuator system or drive motor will increase to maintain a constant speed, so that aerodynamic efficiency becomes a determining factor in maintaining the robot's operational endurance in the campus environment.

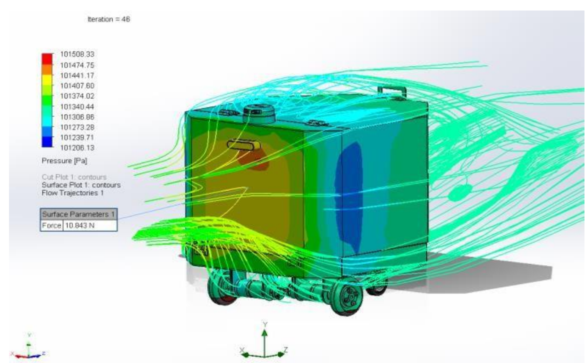

Figure 12 *Visualization Surface Plot and Flow Trajectories Speed 10.0 m/s*

At a maximum test speed of 10.0 m/s (Figure 12), visualization of the flow path shows the formation of a more pronounced wake (air vortex) at the rear of the robot.

Table VII
Results of Force Convergence in the 10.0 m/s Simulation

Parameters	Unit (N)	Averaged Value	Minimum Value	Maximum Value	Convergence
SG Force (Y)	N	4.9931	4.72560	5.0751	Yes
SG Force (Z)	N	12.9906	12.8401	13.380	Yes
Total Equation	N	1.12009	1.10711	1 1.1537	Yes

The data in Table 7 confirms a drastic increase in drag force, reaching 12.9906 N. High frontal pressure and the formation of a low-pressure area at the rear of the robot, which is characteristic of a bluff body, contribute to an increase in the overall drag coefficient value.

2) Quantitative Analysis of Air Resistance and Drag Coefficient

Based on the data presented in Table 3, the simulation results consistently show that drag force (SG Force) increases quadratically with increasing airflow velocity. Aerodynamically, the pressure distribution on the robot body shows a high-pressure zone at the front (stagnation point) and the formation of a low-pressure region (wake region) at the rear. This characteristic is very typical of bluff bodies, where the pressure difference between the front and rear sides is the main contributor to the total drag force, even at low operating speeds. The use of divisor constants in SolidWorks software facilitates consistent automatic calculations across the entire range of speeds tested. This provides a reliable basis for evaluating the drag coefficient (CD), which is a crucial parameter in determining the energy efficiency of robots.

TABLE VIII
Results of Quantitative Analysis of Air Resistance and Drag Coefficient based on Speed Variation.

Speed (v)	Drag Force (Fd)	Coeff. of Drag (Cd)	Description
0.5 m/s	0.023 N	0.80	Highly Efficient
1.5 m/s	0.209 N	0.80	Efficient
2.5 m/s	0.594 N	0.82	Efficient
5.0 m/s	2.159 N	0.74	Starting to Inhibit
10.0 m/s	12.990 N	1.12	High Resistance

Quantitative analysis in Table 8 shows that as the robot's speed increases, the wind load increases significantly, with the drag force jumping from 0.2091 N at a speed of 0.5 m/s to 12.990 N at 10.0 m/s. This drastic increase confirms that the thrust required to overcome aerodynamic drag increases exponentially as the operating speed increases. Although the drag coefficient (CD) tends to be stable, the magnitude of drag force at high speeds remains a critical factor for motor power consumption. As a future improvement, the robot's design can be optimized by giving it a more streamlined shape at the front and adding curves to the sharp corners of the robot's body. This aims to reduce air turbulence and minimize the drag coefficient, so that battery efficiency can be maintained even when the robot is operated at its maximum speed limit.

B. FEA Simulation Loading Scenarios

In this study, three loading scenarios were applied to evaluate the structural performance of the upper body (box) of the delivery robot. Loads of 5 kg, 10 kg, and 15 kg represent the unloaded condition, partial load, and maximum operational load, respectively. The loads were applied vertically downward in the form of pressure to simulate gravitational effects during normal operating conditions.

In this study, three loading scenarios were applied to evaluate the structural performance of the delivery robot's upper body (box). Loads of 5 kg, 10 kg, and 15 kg were defined to represent the unloaded, partial-load, and maximum operational loading conditions, respectively. Each load was applied vertically downward as a pressure load on the upper body to represent the gravitational effect of the carried items during normal operation. The resulting von Mises stress, deformation, and Factor of Safety (FOS) were then evaluated for each loading condition to assess the structural reliability of the upper body under different operational loads.

1) Stress Analysis Results

Stress analysis was conducted to evaluate the structural response of the robot's upper body under different loading conditions. The von Mises stress criterion was employed, as it is widely used to predict yielding in ductile materials such as aluminum.

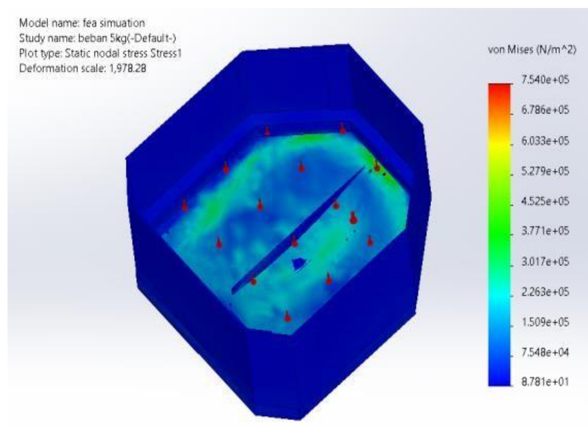

Figure 13 *Analysis of 5kg vertical load stress results*

Figure 13 shows the stress distribution on a 5 kg load. The maximum stress value of 1.069 MPa is concentrated at the main frame joint, which is still well below the material's melting point.

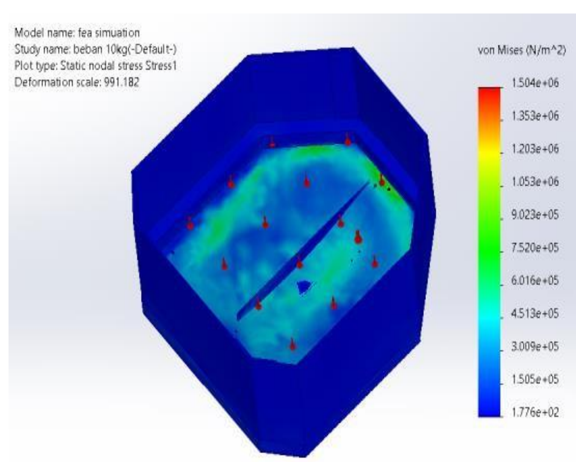

Figure 14 *Analysis of 10kg vertical load stress results*

Figure 14 shows the stress distribution on a 10 kg load. There is an increase in color intensity in the load bearing area with a peak value of 2.138 MPa, but the stress distribution remains uniform throughout the body structure.

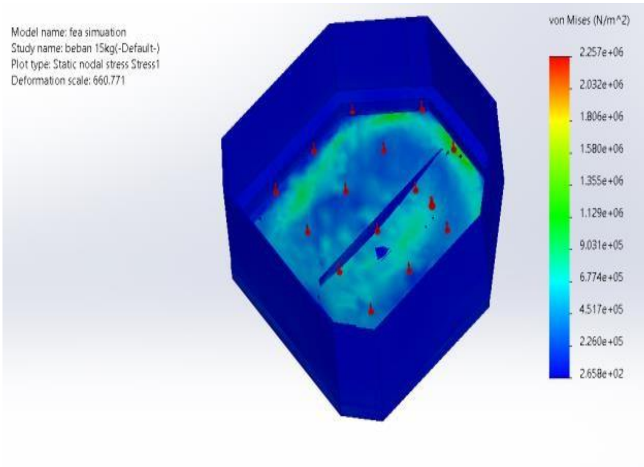

***Figure 15** Analysis of 15kg vertical load stress results*

Figure 15 shows the stress distribution at a maximum load of 15 kg. The stress reaches a peak of 3.207 MPa. Even though the load increases threefold, the structure remains within the elastic zone without the risk of permanent deformation.

The stress analysis results show that the robot frame structure has excellent integrity under various loading conditions. At loads of 5 kg and 10 kg, the resulting stress is very low and evenly distributed throughout the body. However, at the maximum load of 15 kg, there is an increase in more concentrated stress, especially in the joints and main supports that function as force transmission paths. Nevertheless, the maximum stress value is still well below the yield strength of the aluminum material, ensuring that the structure is safe from permanent failure. As a next step in development, it is recommended to perform local reinforcement at critical connection points by adding gussets or selectively thickening the material to increase resistance to long-term dynamic loads without significantly increasing the overall weight of the robot.

2) Displacement Analysis Results

Displacement analysis was performed to evaluate the deformation of the robot's upper box under loading conditions of 5 kg, 10 kg, and 15 kg, representing minimum to maximum operational loads. The resulting displacement was visualized using color maps to illustrate the magnitude and distribution of deformation throughout the structure. The color gradient provides a clear representation of the displacement magnitude, allowing the critical locations experiencing the greatest deflection to be identified. The maximum deformation was generally concentrated at the center of the panel, where the structure was not directly supported by the supporting frame. This condition indicates that the unsupported central region is more susceptible to deformation under applied loading, as shown in the following figure.

The displacement results also indicate a consistent increase in deformation as the applied load increases. This behavior is expected because the structural response is directly influenced by the magnitude of the applied load. Under the 5 kg loading condition, the deformation remains relatively small, indicating that the upper box can withstand the minimum operational load with limited structural movement. As the load increases to 10 kg and 15 kg, the displacement becomes more pronounced, particularly in the unsupported central region of the panel. However, the distribution of deformation remains localized rather than occurring uniformly across the entire upper box. This result provides an important indication of the structural behavior of the box and can be used together with the stress and Factor of Safety analyses to determine whether the design remains within acceptable structural limits for the intended operational loading conditions.

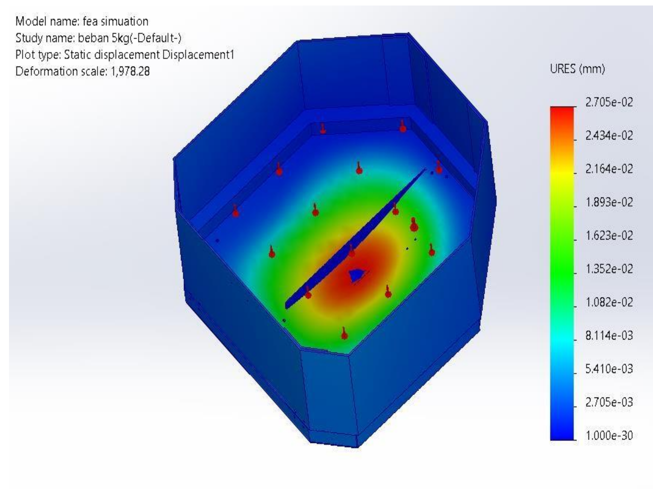

***Figure 16** Displacement analysis results of a 5kg load*

Figure 16 shows body deflection under a 5 kg load. The maximum deformation is only 0.0015 mm, located at the center of the top panel, indicating excellent structural rigidity.

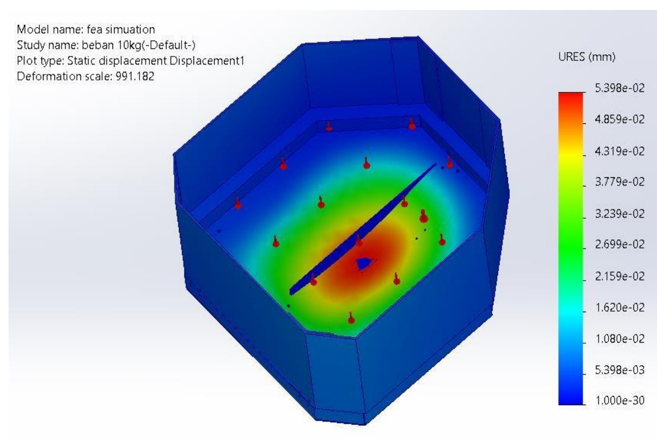

***Figure 17** Displacement analysis results of a 10kg load*

Figure 17 illustrates the body deflection under a 10 kg loading condition. The maximum displacement increases to 0.0030 mm, indicating a very small deformation of the upper box structure. The red region represents the location with the highest displacement, which is concentrated at the most flexible part of the panel. Despite exhibiting the maximum deformation, the displacement remains within the micrometer range (3 µm), indicating that the resulting deformation is very small and is not expected to significantly affect the mechanical function of the robot's upper box under the applied loading condition.

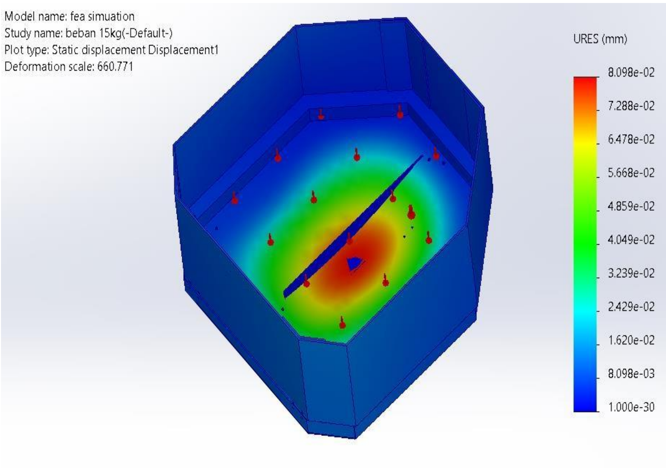

Figure 18 *Displacement analysis results of a 15kg load*

Figure 18 shows body deflection under a 15 kg load. The peak deformation recorded is 0.0045 mm. This proves that even when the maximum working load is applied, the upper box structure of the robot remains stable and does not undergo significant deformation.

The results of the deformation (displacement) analysis show that the upper box structure of the robot has adequate rigidity under various loading conditions. At loads of 5 kg (Figure a) and 10 kg (Figure b), the changes in shape are minimal and are only concentrated in the center of the panel, which has no direct support. When given a maximum load of 15 kg (Figure c), the deformation value did increase, but it remained within safe limits so that it did not interfere with the functionality or stability of the structure as a whole. This confirms that the current robot design is quite sturdy, even though the center of the panel was identified as the most flexible point. As a future improvement measure, long-term structural performance can be enhanced by adding stiffeners to the bottom of the panel or by selectively increasing the thickness of the material to minimize deflection without significantly increasing the vehicle's weight.

3) Safety Factor Evaluation (Factor of Safety)

The factor of safety (FOS) analysis was performed to evaluate the structural reliability of the robot's upper body under operational loads. The results show that the minimum FOS decreases with increasing load, as ex-pected, but remains significantly higher than the common-ly accepted minimum value (FOS > 1).

The decrease in FOS is directly related to the increase in the applied load, which results in higher stress within the upper body structure. Under the 5 kg loading condition, the structure exhibits the highest safety margin, while the 10 kg and 15 kg loading conditions produce progressively lower FOS values. Despite this reduction, the minimum FOS at the maximum operational load remains substantially above unity, indicating that the structure has sufficient capacity to withstand the applied loading conditions without reaching the material failure limit. The FOS distribution also shows that the critical regions are concentrated around areas experiencing higher stress, particularly near the unsupported sections of the upper box. These results demonstrate that the upper body maintains adequate structural reliability across the evaluated loading scenarios and provides a sufficient safety margin for the intended operational conditions.

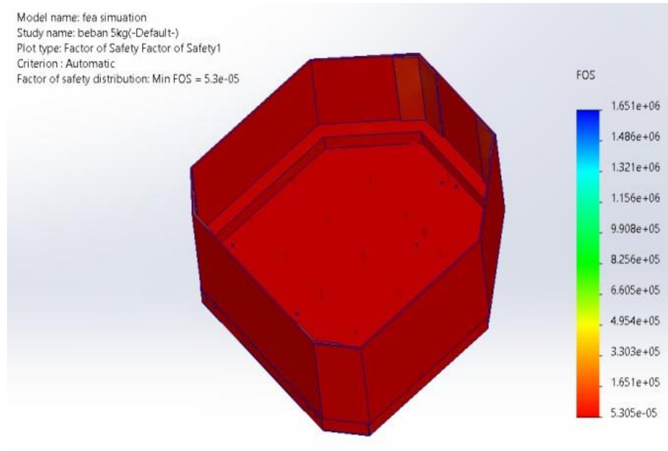

Figure 19 *Results of FOS analysis load from a 5kg load*

Figure 19 shows the safety factor distribution under a 5 kg loading condition. Most of the structure is represented by the blue region, indicating a high Factor of Safety (FOS) value exceeding 15. This result demonstrates that the upper body has a substantial safety margin under the 5 kg load. The high FOS indicates that the applied load generates stress levels that remain far below the material's allowable strength, suggesting that the Aluminium 6061 structure is capable of safely supporting the minimum operational load without approaching its failure limit.

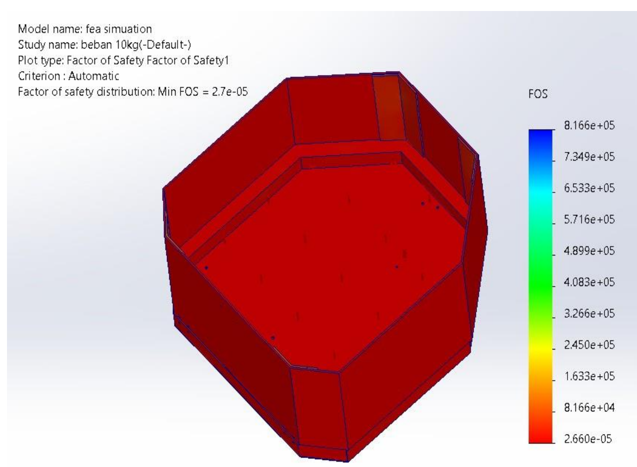

Figure 20 *Results of FOS analysis from a 10kg load*

Figure 20 shows the safety factor map at a load of 10 kg, providing a spatial distribution of the structural reliability across the robot frame. The FOS value begins to decrease slightly in the joint areas and critical connection points due to localized stress concentration; however, it remains at a very conservative level, far exceeding the standard industrial safety requirements. This high margin of safety ensures the body's resistance to unpredictable shock loads or vibrations that may occur during campus navigation on uneven surfaces. The predominantly blue regions in the visualization indicate that the majority of the structure operates under minimal mechanical distress, suggesting that the 10 kg load is well within the safe operational envelope of the Aluminium 6061 framework.

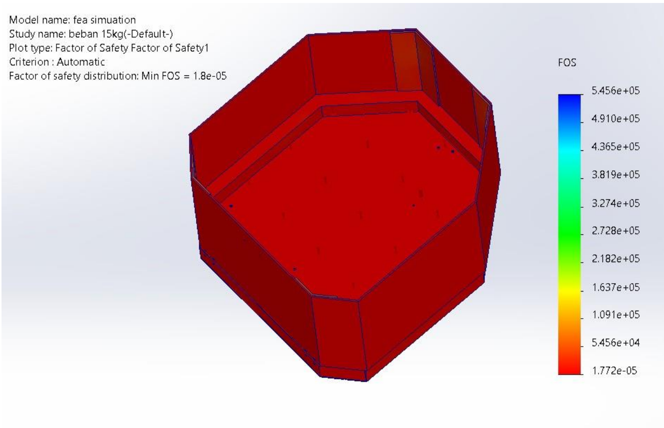

Figure 21 *Results of FOS analysis from a 15kg load*

Figure 21 shows the safety factor map at a load of 15 kg. The lowest FOS value recorded is 85.7. This confirms that this robot is significantly overdesigned for a load of 15 kg and is capable of withstanding loads far greater than its current operational capacity.

The safety factor evaluation shows that the robot's upper box structure has a very high level of safety under all load conditions analyzed. At loads of 5 kg (Figure a), 10 kg (Figure b), and up to the maximum load of 15 kg (Figure c), the Factor of Safety (FOS) value remains well above the minimum required limit, confirming that the stresses occurring are still within the elastic limits of the material. While this ensures exceptional structural safety, the very high FOS value also indicates that the current design tends to be overdesigned or structurally excessive. Therefore, future design optimization can be achieved by reducing the material thickness in areas with low stress or simplifying the frame geometry to improve material efficiency and reduce the overall weight of the robot without compromising operational safety standards.

4) *Discussion of Structural Performance*

The structural performance evaluation indicates that increasing the load results in proportional increases in stress and displacement. However, even at the maximum operational load of 15 kg, the structure exhibits low stress levels, minimal deformation, and a very high factor of safety.

The table shows that increasing load results in a proportional rise in maximum stress and displacement, from 0.676 MPa and 0.024 mm at 5 kg to 0.754 MPa and 0.027 mm at 10 kg, and reaching 1.50 MPa and 0.054 mm at 15 kg. These results confirm that the upper body structure has sufficient strength and rigidity to safely withstand operational loads without yielding or excessive deformation. The FEA analysis results confirm the robot's exceptional structural integrity. However, the FOS value of 85.7 indicates potential material waste. Recommendations for further development include topology optimization or reducing the thickness of aluminum plates in areas with low stress to reduce the robot's total weight, thereby improving battery efficiency without compromising safety.

IV. CONCLUSION

This study successfully evaluated the aerodynamic performance and structural integrity of the campus delivery robot design through numerical analysis. Simulation results show that although drag force increases quadratically with speed, its effect remains minimal at standard campus operating speeds (1.5–2.5 m/s). From a structural standpoint, the design was deemed very safe with a high Safety Factor even at a maximum load of 15 kg. In conclusion, this design is ready for production, with the caveat that material optimization is needed in areas with low stress to improve weight efficiency.

ACKNOWLEDGMENT

The author would like to express his deepest gratitude to the Department of Electrical Engineering, particularly the Robotics Engineering Technology Study Program, Batam State Polytechnic, for the laboratory facilities and technical guidance provided during this research. The author would also like to express his appreciation to the team and lecturers who have provided valuable input in completing the design and simulation of this robot. This research is expected to make a tangible contribution to the development of delivery robot technology in the campus environment.

REFERENCES

[1] J. Li, X. Zhu, C. Zhang, S. Dang, and G. Chen, “CFD simulation of passenger car aerodynamics and body parameter optimization,” Fluid Dyn. Mater. Process., vol. 21, no. 9, pp. 1845–1862, 2025.

[2] A. Valencia and N. Lepin, “Effect of spoilers and diffusers on the aerodynamics of a sedan automobile,” Int. J. Heat Technol., vol. 42, no. 4, pp. 1164–1172, 2024.

[3] A. Guerrero, R. Castilla, and G. Eid, “A numerical aerodynamic analysis on the effect of rear underbody diffusers on road cars,” Appl. Sci., vol. 12, no. 8, p. 3763, 2022.

[4] G. Liao, M. Xue, L. Yue, H. Yang, P. Guo, X. Hu, Z. Wang, and T. Ma, “Passive drag reduction optimization for complex commercial vehicle models,” J. Appl. Fluid Mech., vol. 18, no. 6, pp. 1639–1651, 2025, doi: 10.47176/jafm.18.6.2983.

[5] A. K. Ary, A. R. Prabowo, and F. Imaduddin, “Structural assessment of an energy-efficient urban vehicle chassis using finite element analysis—A case study,” Procedia Struct. Integr., vol. 27, pp. 69–76, 2020.

[6] O. Zamzam, A. A. Ramzy, M. Abdelaziz, T. Elnady, and A. A. Abd El-Wahab, “Structural performance evaluation of electric vehicle chassis under static and dynamic loads,” Sci. Rep., vol. 15, p. 5168, 2025, doi: 10.1038/s41598-025-86924-w.

[7] M. F. Andira, W. Afnison, W. Waskito, and D. Y. Sari, “Comparative static structural assessment of an energy-efficient prototype vehicle chassis using finite element analysis: AISI 1020 steel vs. 6061-T6 aluminum,” J. Eng. Res. Lecturer, vol. 4, no. 3, pp. 146–158, 2025, doi: 10.58712/jerelv4i3.199.

[8] Y. Liu, C. Liu, X. Gao, and J. Tan, “Multiphysics finite element analysis and optimization of load-bearing frame for pure electric SUVs,” Symmetry, vol. 17, no. 7, p. 1143, 2025, doi: 10.3390/sym17071143.

[9] W. P. S. Simanjuntak and A. Wibisana, “Depth camera-based human detection using YOLOv5,” in Proc. 2nd Int. Conf. Appl. Mech. Eng. Green Technol., Cham, Switzerland: Springer, 2024, pp. 151–162.

[10] V. N. Perkasa, M. T. Silalahi, I. Wijayanti, and H. Widiastuti, “Computational fluid dynamics analysis of marine propeller hydrodynamic performance: A systematic investigation across extended operational envelopes,” in Proc. 2nd Int. Conf. Appl. Mech. Eng. Green Technol., Cham, Switzerland: Springer, 2024, pp. 445–455.

[11] J. Sun and C. Zhou, “Optimising aerodynamic drag for enhanced robotic balancing,” Eng. Appl. Comput. Fluid Mech., vol. 18, no. 1, p. 2430659, 2024, doi: 10.1080/19942060.2024.2430659.

[12] A. Sameh and A. M. Elhenidy, “Bio-inspired underwater robotic vehicle for marine exploration and AI-powered fish detection,” Discover Appl. Sci., vol. 8, p. 117, 2026, doi: 10.1007/s42452-025-07991-2.

[13] A. Welch-Phillips, D. Gibbons, D. P. Ahern, and J. S. Butler, “What is finite element analysis?” Clin. Spine Surg., vol. 33, no. 8, pp. 323–324, 2020.

[14] S. El Fakkoussi, S. Vlase, M. Marin, O. Koubaiti, A. Elkhalfi, and H. Moustabchir, “Predicting stress intensity factor for aluminum 6062 T6 material in L-shaped lower control arm (LCA) design using extended finite element analysis,” Materials, vol. 17, no. 1, p. 206, 2023, doi: 10.3390/ma17010206.

[15] A. Berardi, C. D. Dellisanti, D. Tarantino, K. S. Leheche Ouette, A. Leone, and A. Tamborrino, “FEA for optimizing design and fabrication of frame structure of elevating work platforms,” Appl. Sci., vol. 15, no. 13, p. 7356, 2025, doi: 10.3390/app15137356.

[16] M. Ribfli, A. Wibisana, and T. A. N. C. During, “Analysis of the structural strength of the Barelang63 wheeled robot goalkeeper frame for ball impact and robot load using finite element analysis (FEA),” in Proc. 2nd Int. Conf. Appl. Mech. Eng. Green Technol., Cham, Switzerland: Springer, 2024, pp. 509–520.

[17] A. Wibisana, M. I. Shodiq, M. N. A. Diputra, and N. Nazhifah, “Performance comparison of wheeled soccer robot frames using finite element analysis (FEA),” J. Integrasi, vol. 17, no. 1, pp. 59–69, 2025.

[18] H. D. Anggara, “Revitalizing vehicle innovation: Exploring electric car chassis structures through finite element analysis,” Innovation Eng., vol. 1, no. 1, pp. 50–59, 2024.

[19] I. G. Wiratmaja, N. A. Wigraha, and K. Purnayasa, “Analisis tegangan statik dan deformasi frame Electric Ganesha Scooter Portable (E-GASPOL) menggunakan software SolidWorks,” Otopro, vol. 19, no. 1, pp. 8–17, 2023.

[20] T. Deemyad and R. Moeller, “Chassis design and analysis of an autonomous ground vehicle (AGV) using genetic algorithm,” in Proc. 2020 Intermountain Eng., Technol. Comput. (IETC), 2020, pp. 1–6.

[21] T. Zhu and J. Xiang, “Chassis design of tomato picking robot in the greenhouse,” J. Phys.: Conf. Ser., vol. 2136, no. 1, p. 012047, 2021.

[22] A. Rajurkar, K. Dangra, A. Deshpande, M. Gosavi, T. Phadtare, and G. Gambhire, “Comparative finite element analysis of a novel robot chassis using structural steel and aluminium alloy materials,” Eng. Innovations, vol. 7, pp. 61–73, 2023.

[23] A. Nuramal, H. Hestiawan, and R. D. E. Putra, “Finite element analysis of thermal and structural behavior in food packaging machinery using ANSYS,” in Proc. 2nd Int. Conf. Appl. Mech. Eng. Green Technol., Cham, Switzerland: Springer, 2024, pp. 319–330.

[24] M. Koehler, A. M. Okamura, and C. Duriez, “Stiffness control of deformable robots using finite element modeling,” IEEE Robot. Autom. Lett., vol. 4, no. 2, pp. 469–476, 2019.